


 Cite this: *Nanoscale*, 2024, **16**, 12037

A gold nanocluster/MIL-100(Fe) bimodal nanovector for the therapy of inflammatory disease through attenuation of Toll-like receptor signaling†

Heng Zhao,^a Sonia Becharef,^b Eddy Dumas,^c Florent Carn,^b Gilles Patriarche,^d Simona Mura,^b Florence Gazeau,^b *^b Christian Serre,^b *^a and Nathalie Steunou,^b *^{a,c}

A better understanding of the molecular and cellular events involved in the inflammation process has opened novel perspectives in the treatment of inflammatory diseases, particularly through the development of well-designed nanomedicines. Here we describe the design of a novel class of anti-inflammatory nanomedicine (denoted as Au@MIL) synthesized through a one-pot, cost-effective and green approach by coupling a benchmark mesoporous iron(III) carboxylate metal organic framework (MOF) (*i.e.* MIL-100 (Fe)) and glutathionate protected gold nanoclusters (*i.e.* Au₂₅SG₁₈ NCs). This nano-carrier exhibits low toxicity and excellent colloidal stability combined with the high loading capacity of the glucocorticoid dexamethasone phosphate (DexP) whose pH-dependent delivery was observed. The drug loaded Au@MIL nanocarrier shows high anti-inflammatory activity due to its capacity to specifically hinder inflammatory cell growth, scavenge intracellular reactive oxygen species (ROS) and downregulate pro-inflammatory cytokine secretion. In addition, this formulation has the capacity to inhibit the Toll-like receptor (TLR) signaling cascade namely the nuclear factor kappa B (NF-κB) and the interferon regulatory factor (IRF) pathways. This not only provides a new avenue for the nanotherapy of inflammatory diseases but also enhances our fundamental knowledge of the role of nanoMOF based nanomedicine in the regulation of innate immune signaling.

Received 31st December 2023,
Accepted 13th May 2024

DOI: 10.1039/d3nr06685a
rsc.li/nanoscale

1. Introduction

Inflammation is a complex immune response to potentially harmful stimuli such as pathogens, tissue damage or metabolic stress. It plays a protective role in the host system as a result of a balanced inflammatory response allowing clearance of injured tissue and pathogens with minimal damage to host cells. However, chronic and uncontrolled inflammatory responses may become harmful and damaging for the tissues, thereby leading to the development and pathogenesis of

chronic inflammatory diseases such as rheumatoid arthritis (RA).¹ As an incurable chronic autoimmune inflammatory disease, RA is characterized by synovial joint inflammation and irreversible destruction of cartilage and bone tissue, which can lead to disability, inability to participate in work and social activities, and also increased mortality.^{2–4} One of the main clinical pathological features is the infiltration of inflammatory macrophages in joints leading to synovial hyperplasia. Moreover, these are responsible for the release of some proinflammatory factors such as tumor necrosis factor-α (TNF-α), interleukin-1β (IL-1β), and interleukin-6 (IL-6), resulting in bone erosion and cartilage tissue damage.^{1–6} In recent years, cellular and molecular advances have improved the understanding of the inflammatory process, allowing the discovery of multiple targets for the therapy of inflammatory diseases. Therefore, in addition to a variety of quite effective anti-inflammatory agents already available, such as non-steroidal anti-inflammatory drugs (NSAIDs), glucocorticoids and disease-modifying anti-rheumatic drugs (DMARDs), many biological agents have also been developed including antibodies and nucleic acids.^{2–4} Although promising progress has been made

^aInstitut des Matériaux Poreux de Paris, ENS, ESPCI Paris, CNRS, PSL University, Paris, France. E-mail: christian.serre@ens.fr, nathalie.steunou@uvsg.fr

^bUniversité Paris Cité, MSC UMR CNRS 7057, 75006 Paris, France.

E-mail: florence.gazeau@univ-paris-diderot.fr

^cInstitut Lavoisier de Versailles, UMR CNRS 8180, Université de Versailles St Quentin en Yvelines, Université Paris Saclay, Versailles, France

^dUniversité Paris-Saclay, CNRS, Centre de Nanosciences et de Nanotechnologies, 91120 Palaiseau, France

^eUniversité Paris-Saclay, CNRS, Institut Galien Paris-Saclay, 91400 Orsay, France

† Electronic supplementary information (ESI) available. See DOI: <https://doi.org/10.1039/d3nr06685a>

in developing such treatments, the non-specific biodistribution, short biological half-life and poor bioavailability of these drugs associated with the widespread distribution of the inflammatory signaling pathways in multiple cell types and tissues have led to high and frequent drug administration which often causes severe side effects.^{1–6} To overcome these limitations, encapsulation of active ingredients in nanocarriers such as liposomes was developed to enhance drug absorption and biodistribution in inflammatory sites as well as to reduce their toxicity.^{1–6} However, to date, the clinical translation of these anti-inflammatory nanotherapeutics is still hampered by their poor stability in biological fluids, low drug loading and uncontrolled drug delivery as well as hurdles in their large scale and cost-effective production. More importantly, these treatments are generally based on single-target drugs while multiple mechanisms and signaling pathways are involved in inflammatory diseases such as RA.^{1–6} Therefore, there is an urgent need to develop alternative drug nanomedicines combining different anti-inflammatory modalities to target different signaling pathways and thus improve the treatment of inflammatory disease.

In the present article, we describe the design of a novel anti-inflammatory nanocarrier (denoted as Au@MIL) based on atomically precise glutathione protected Au₂₅(I) nanoclusters (Au₂₅SG₁₈ NCs) assembled with a mesoporous Fe(III) tricarboxylate nanoMOF (*i.e.* MIL-100(Fe)). MOFs are crystalline porous materials constructed by assembling diverse inorganic building units (metal ions, clusters and chains) with polydentate organic ligands. Their large surface area, amphiphilic internal microenvironment and their possible functionalization make these materials suitable to host a large variety of drugs with excellent loading capacities.^{7–14} Their high chemical and structural diversity can confer to these nanocarriers valuable features such as progressive and eventually stimuli-responsive drug release properties as well as complementary functionalities of interest for diagnosis and imaging.^{15–21} Note that MOFs have been mainly explored to date for cancer therapy and their performance in therapies of inflammatory diseases such as RA has only recently been reported.^{22–26}

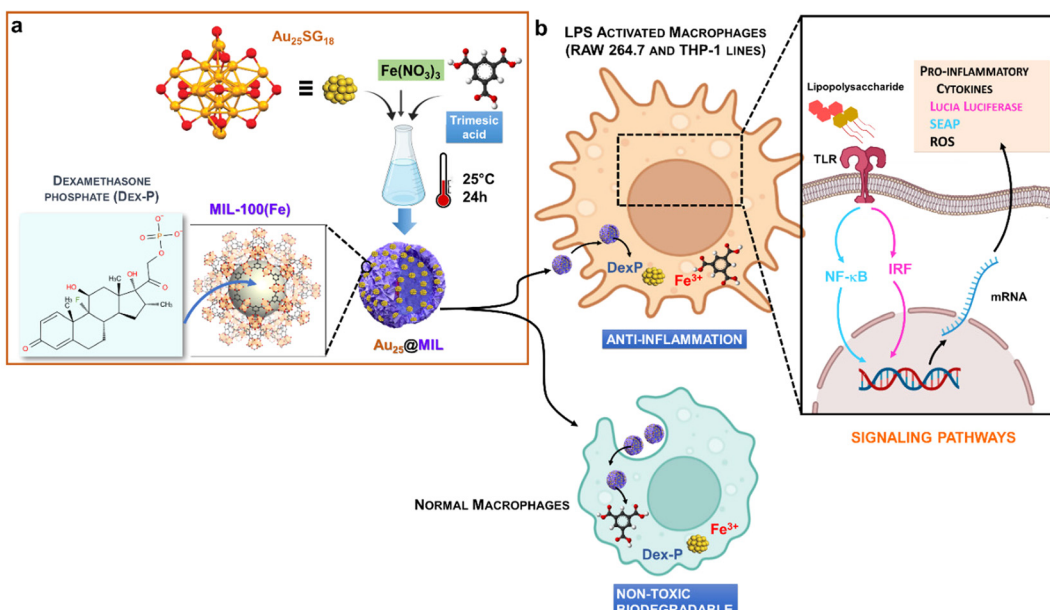
In this study, MIL-100(Fe) nanoparticles (NPs) were combined with Au₂₅ NCs due to their excellent biocompatibility, high colloidal and chemical stability and anti-inflammatory capability. It is noteworthy that Au NPs and NCs have been previously shown to inhibit the activation of the NF-κB pathway, reducing the production of ROS and the secretion of pro-inflammatory cytokines, thereby limiting the inflammation-induced bone and cartilage destruction.^{27,28} Moreover, MIL-100(Fe) was recently shown to exhibit good anti-inflammatory capacity which might be imparted by their fast internalization in macrophages and the high Fe³⁺ intracellular concentration.²⁶ Its assembly with Au₂₅SG₁₈ NCs together with the loading of glucocorticoid dexamethasone phosphate (that is Au@MIL/Dex-P) has led to a nanomedicine with a high anti-inflammatory efficacy as a result of its activity on different therapeutic targets. The use of an anti-inflammatory screening cell model (*i.e.* THP1-DualTM derived macrophages) allowed us to demonstrate the inhibition of Toll-like receptor (TLR) sig-

naling such as the nuclear factor kappa B (NF-κB) and interferon regulatory factor (IRF) pathways.

2. Results and discussion

2.1 Synthesis and characterization of Au₂₅@MIL nano-objects

The hybrid gold nanocluster – MIL-100(Fe) nano-object (denoted as Au₂₅@MIL) was prepared through an *in situ* room temperature (RT) green synthesis of MIL-100(Fe) by mixing the pre-synthesized Au₂₅SG₁₈ NCs with the precursors of MIL-100(Fe), namely Fe(NO₃)₃ and trimesic acid (BTC) in water (Scheme 1 and the ESI† for experimental details). We have selected this strategy rather than the possible direct mixing of preformed MIL-100(Fe) NPs with Au₂₅SG₁₈ NCs. Indeed, the *in situ* strategy is expected to entrap the Au₂₅SG₁₈ NCs in the 3D assembly of MOF nanocrystals and this might lead to a high stabilization and spatial distribution of gold nanoclusters within MOF NPs, as previously shown for numerous MOF based composites.²⁹ The RT synthesis of MIL-100(Fe) was previously reported by some of us.^{26,30,31} Au₂₅SG₁₈ NCs were synthesized by a glutathione (GSH) etching method as previously reported.^{32,33} The diameter of these Au₂₅SG₁₈ NCs is 1.6 ± 0.3 nm as shown by transmission electron microscopy (TEM) (Fig. S1†). Results of their characterization by ultraviolet-visible (UV-Vis) and fluorescence (FL) emission spectra (Fig. S1†) are fully consistent with that previously reported.^{32,33} Au₂₅(X)@MIL nano-objects were prepared with different Au₂₅SG₁₈ contents (from X = 3 to 25 wt%) by tuning the initial amount of Au₂₅SG₁₈ NCs used in the synthesis. This Au₂₅SG₁₈ content was determined by inductively coupled plasma mass spectrometry (ICP-MS) (Table S1†). Au₂₅(X)@MIL NPs were further characterized by powder X-ray diffraction (PXRD), thermogravimetric analysis (TGA), nitrogen porosimetry at 77 K, TEM, high angle annular dark field mapping in scanning transmission electron microscopy (STEM-HAADF) and energy dispersive X-ray spectroscopy (EDS) mapping (Fig. 1 and 2). We have shown that the loading rate of Au₂₅SG₁₈ NCs could not exceed 13 wt%, beyond which a decrease in the crystallinity and porosity of the MOF was observed. We thus characterized more deeply Au₂₅(X)@MIL with two different Au₂₅SG₁₈ NCs loadings (X = 3 and 13 wt%). The PXRD patterns of Au₂₅(3)@MIL and Au₂₅(13)@MIL nano-objects display the characteristic Bragg peaks of MIL-100(Fe) with the absence of any decrease of crystallinity upon embedding Au₂₅SG₁₈ NCs into MIL-100(Fe) (Fig. 1a). Due to the ultrasmall diameters of Au₂₅SG₁₈ NCs, no PXRD peak of Au NCs was observed in the pattern. In Fig. S2 and S3,† the FT-IR spectra and TGA profiles of Au₂₅(X)@MIL are comparable to that of bare MIL-100(Fe) due to the large amount of the MOF in those nano-objects. According to N₂ porosimetry results, Au₂₅(3)@MIL and Au₂₅(13)@MIL present a high porosity as shown by their Brunauer–Emmett–Teller (BET) area of 1650 ± 6 m² g⁻¹ and 1427 ± 6 m² g⁻¹ respectively. The BET area of Au₂₅(13)@MIL is as expected lower than that of Au₂₅(3)@MIL and bare MIL-100



Scheme 1 Schematic illustration of (a) the synthesis of Au₂₅@MIL-100(Fe) nano-objects and (b) their use as a platform for the therapy of inflammatory diseases. LPS: lipopolysaccharide; TLR: Toll-like receptor; ROS: reactive oxygen species; DexP: dexamethasone phosphate; IRF: interferon regulatory factor pathway; NF-κB: nuclear factor kappa B pathway; SEAP: secreted embryonic alkaline phosphatase.

(Fe) NPs ($1720 \pm 6 \text{ m}^2 \text{ g}^{-1}$), due to the presence of a larger amount of Au₂₅SG NCs (Fig. 1b). As shown in Fig. 1c, the pore size distribution of Au₂₅(3)@MIL and Au₂₅(13)@MIL is similar to that of bare MIL-100(Fe) (two types of mesoporous cages of *ca.* 25 Å and 29 Å)³⁴ (Fig. 1c), indicating the successful formation of MIL-100(Fe) in the presence of Au₂₅SG₁₈ NCs. Moreover, the two mesoporous cages of MIL-100(Fe) in the Au₂₅(X)@MIL nano-objects are still accessible to N₂ and are thus presumably not occupied by Au₂₅SG₁₈ NCs. Such nano-objects are thus prone to encapsulating drugs with a high loading capacity. According to TEM, STEM-HAADF and EDS mapping (Fig. 2 and S4–S7 of ESI†), the Au₂₅(3)@MIL and Au₂₅(13)@MIL nano-objects consist of MIL-100(Fe) NPs with a diameter of about 40 nm whose surface is decorated by Au₂₅SG₁₈ NCs, and very small Au NPs, with diameters up to 2 nm (Fig. 2 and S4, S5†). The microstructure of such nano-objects presumably results from coordination bonds between surface Fe(III) of MIL-100(Fe) and pendant carboxyl and amino functions of Au₂₅SG₁₈ NCs as previously shown for an Fe³⁺ photoluminescence sensor based on GSH-Au NCs.^{35,36} One cannot also exclude that some Au NCs and NPs are also embedded into the MOF nanocrystals. The TEM images clearly indicated that Au₂₅SG₁₈ NCs and/or Au NPs with a high crystallinity were homogeneously distributed at the surface of MIL-100(Fe) NPs (Fig. 2a–c & S5†).

For the following steps, Au₂₅(13)@MIL with the highest Au content was selected to investigate the combined effect of MIL-100(Fe) and Au₂₅SG₁₈ NCs on the anti-inflammatory activity.

The colloidal stability of Au₂₅(13)@MIL was firstly investigated by dynamic light scattering (DLS) in aqueous solutions

at different pH (Fig. S8†). Good colloidal stability of Au₂₅(13)@MIL was observed at pH ranging between 4 and 6 as a result of its small mean diameter (~150 nm at pH 5–6). In contrast, a partial and strong aggregation of this nano-object was respectively observed at pH 7 and 3, in agreement with a decrease of its surface charge as previously reported for pure MIL-100(Fe)³⁷ (Fig. S8b†). Furthermore, the colloidal stability of Au₂₅(13)@MIL was studied under different simulated physiological media conditions, including Milli Q water (MQ H₂O), neutral phosphate buffered saline (PBS), NaCl solution (0.9% NaCl), Dulbecco's modified Eagle's medium (DMEM) cell culture medium, and DMEM supplemented with fetal bovine serum (FBS) (90/10% v/v) medium (DMEM + FBS). In contrast to very fast aggregation observed in DMEM and 0.9% NaCl, the aggregation process of Au₂₅(13)@MIL is observed after 4 hours in neutral PBS. However, Au₂₅(13)@MIL nano-objects showed an excellent colloidal stability in MQ H₂O and DMEM + FBS since their hydrodynamic diameter of ~150 nm remained constant for 24 h (Fig. S9†). This enhanced colloidal stability of Au₂₅(13)@MIL may result from the adsorption of bovine serum albumin at the surface of these nano-objects as previously observed for MIL-100(Fe) and γFe₂O₃/MIL-100(Fe) nanocarrier.^{26,37,38}

2.2 Surface modification of Au₂₅(13)@MIL: impact on their pH- and GSH responsive release properties

To design a drug delivery system, a high drug loading capacity combined with sustained stimuli-triggered drug release property is desirable to better control the biodistribution and bioavailability of the drug at the target site and thus limit the amount of carrier material.³⁹ Herein we advantageously used

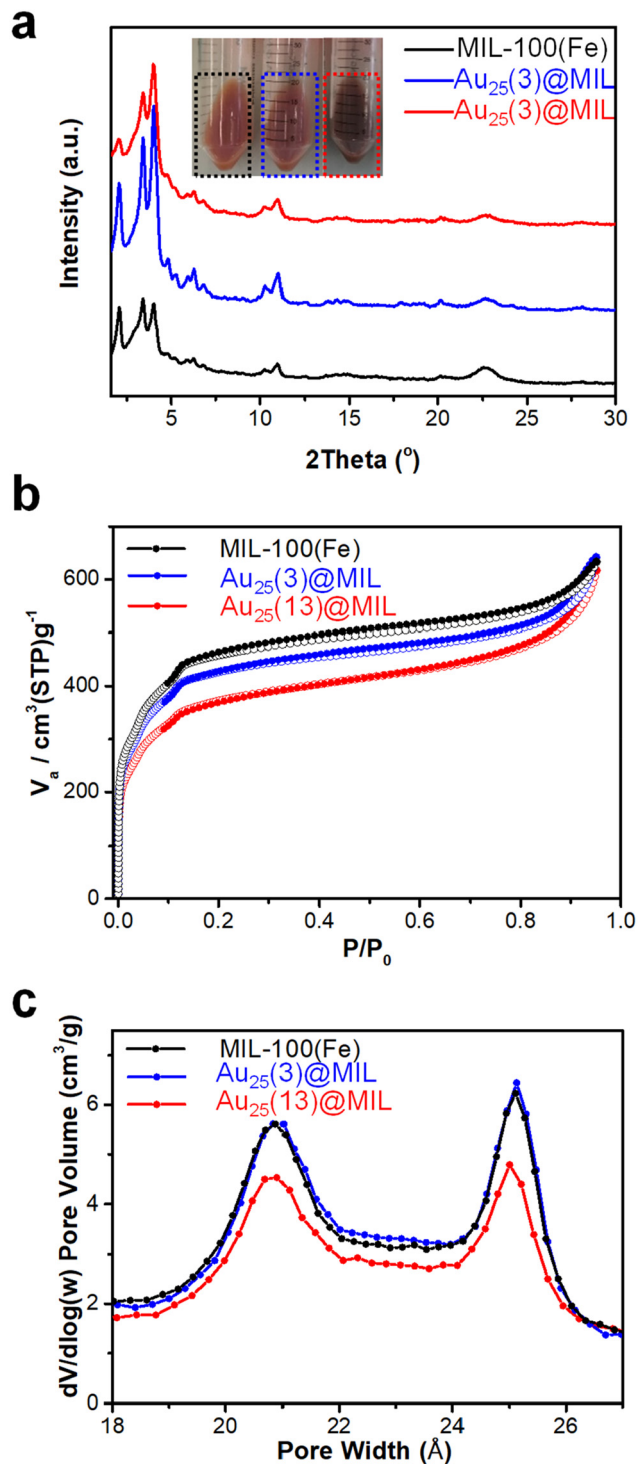


Fig. 1 Characterizations of $\text{Au}_{25}(X)@\text{MIL}$. (a) PXRD patterns ($\lambda_{\text{Cu}} = 1.5406 \text{ \AA}$), (b) nitrogen sorption isotherms at 77 K ($P_0 = 1 \text{ atm}$) and (c) pore size distribution (PSD) derived from the Barrett–Joyner–Halenda (BJH) pore size model of MIL-100(Fe), $\text{Au}_{25}(3)@\text{MIL}$ and $\text{Au}_{25}(13)@\text{MIL}$.

the preserved porosity of MIL-100(Fe) in $\text{Au}_{25}(13)@\text{MIL}$ to investigate the drug loading and release properties of this nano-object in physiological media. Clinically, RA is often treated with glucocorticoids. In particular, dexamethasone

(Dex) is a potent corticosteroid with gluconeogenic, immunosuppressive and anti-inflammatory properties.⁴ The encapsulation of Dex in a few MOFs such as ZIF-8,^{40,41} Zn–Mg-MOF-74⁴² and γ -cyclodextrin-MOF^{43,44} was previously explored for the development of bone implants or the treatment of eye inflammation. Moderate Dex loading capacity (LC) values ranging between ~ 6 and ~ 16 wt% and sustained release in PBS for a few weeks could be achieved by using these MOFs. Notably, the Dex LC value of ZIF-8 can reach a high value up to 80 wt%⁴⁵ but the intrinsic poor chemical stability of ZIF-8 in phosphate buffered saline (PBS) or under acidic intracellular conditions is detrimental for biomedical applications.⁴⁶ Here we have selected Dex bearing a phosphate group (*i.e.* dexamethasone phosphate, DexP) in order to enhance the interactions with MIL-100(Fe) through the possible coordination of the phosphate group with the coordinatively unsaturated Fe(III) sites. This strategy was previously used for the encapsulation of azidothymidine triphosphate (AZT-TP) in MIL-100(Fe).⁴⁷ This specific host–guest interaction is prone to enhance the drug loading and may lead to a progressive drug release. Herein, DexP was encapsulated in MIL-100(Fe) and $\text{Au}_{25}(13)@\text{MIL}$ *via* the direct immersion of NPs in DexP aqueous solution. The drug LC of MIL-100(Fe) and $\text{Au}_{25}(13)@\text{MIL}$ was equal to ~ 49 wt% and ~ 43 wt% respectively for an initial weight ratio of MOF : DexP = 1 : 0.5 according to high-performance liquid chromatography (HPLC) values (Fig. S10 and Table S2†). A slightly higher DexP LC of 46 wt% in $\text{Au}_{25}(13)@\text{MIL}$ was achieved by increasing the DexP amount (*i.e.* MOF : DexP = 1 : 1). Importantly, the PXRD patterns of MIL-100/DexP and $\text{Au}_{25}(13)@\text{MIL}/\text{DexP}$ are consistent with that of MIL-100(Fe) (Fig. S11†), indicating that the crystalline structure of MIL-100(Fe) is preserved upon the encapsulation of DexP. The encapsulation of DexP in the mesopores of MIL-100(Fe) was also confirmed by N_2 porosimetry since the BET area of $\text{Au}_{25}(13)@\text{MIL}/\text{DexP}$ at both 43 and 46 wt% LC decreased dramatically (Fig. S12†). According to the pore size distribution derived from the BJH pore-size model (Fig. S12b and d†), DexP molecules most likely occupy the large mesopores of MIL-100(Fe) while a few DexP molecules might also be present in the small mesoporous cages of the MOF. In the next steps, $\text{Au}_{25}(13)@\text{MIL}/\text{DexP}$ prepared with a MOF : DexP = 1 : 0.5 weight ratio was considered due to the high DexP LC achieved for a minimal amount of DexP used.

Glucocorticoid therapy is associated with multiple serious adverse effects in a dose-dependent manner, and it is thus of primary importance to achieve efficient drug delivery from the circulation to the target inflammatory tissues. It is worth noting that endosomal–lysosomal system of normal tissues and the synovial tissue of patients with RA are in a low-pH environment in comparison with blood (pH 7.4) and are characterized by an alteration of the regulation of glutathione (GSH, L- γ -glutamyl-L-cysteinylglycine) levels.^{48–50} GSH is a vital antioxidant found in the human body, protecting cellular elements from damage caused by free radicals. Moreover, the variations in GSH concentrations between the extracellular (~ 2 – $10 \mu\text{M}$) and intracellular (~ 2 – 10 mM) compartments were

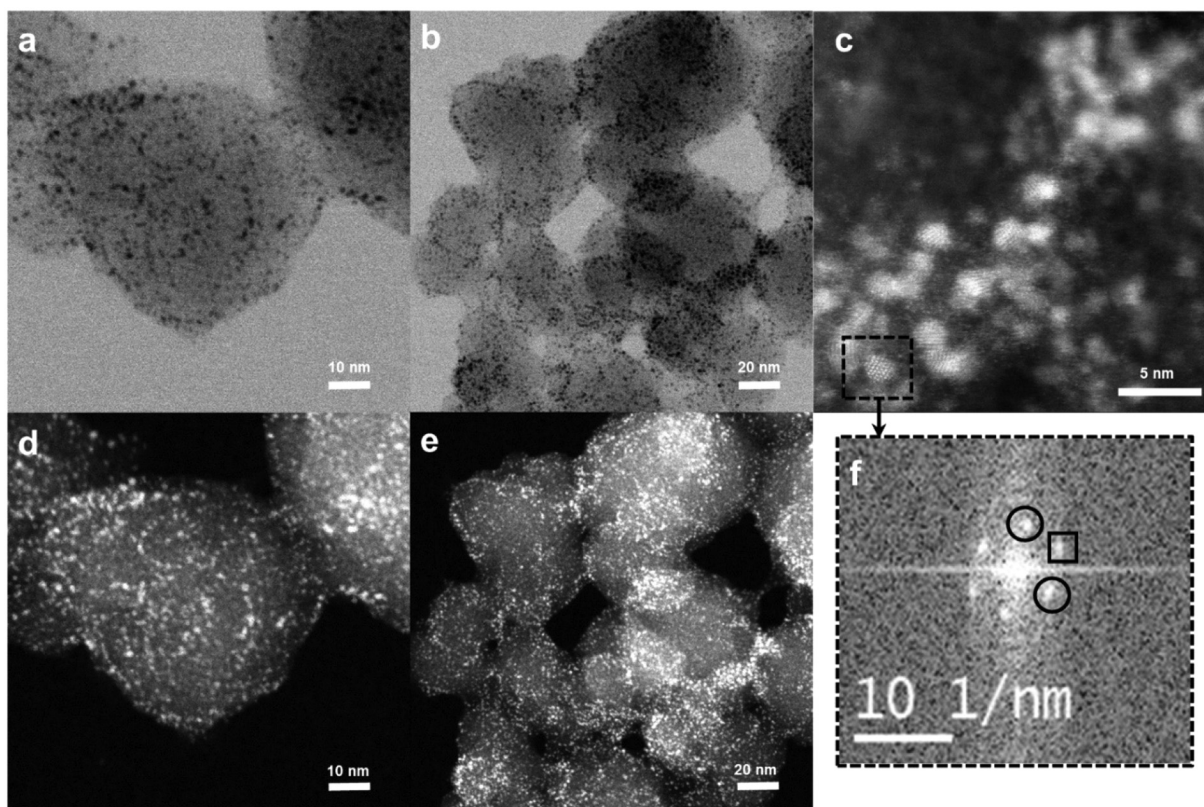


Fig. 2 (a and b) Bright field STEM images and (c–e) HAADF-STEM images obtained at different magnifications. (f) Gives the Fourier transform of an area centered on a specific crystallite of the image (c). From the FT pattern, the crystallite could be identified as a gold crystallite in a $\langle 100 \rangle$ zone axis of the face-centered cubic structure. The two spots surrounded by a circle that correspond to 111 planes were measured at 0.221 and 0.241 nm for a theoretical inter-planar spacing of 0.235 nm. The spot surrounded by a square is then identified as a 200 spot, given an inter-planar spacing of 0.201 nm (for a theoretical value of 0.204 nm).

previously utilized as endogenous stimuli to trigger drug release.^{48–50} As shown in Fig. 3b, the release rate of DexP from $\text{Au}_{25}(13)@\text{MIL}$ /DexP greatly depends on pH since a faster release occurs in neutral PBS while a sustained release is observed in acidic pH. At pH 7.4, 52%, 73% and 86% DexP were released after 1, 4 and 8 h, respectively. The release of DexP is substantially slowed down in PBS (pH 5.1) and PBS (pH 5.1) containing 10 mM GSH (PBS + GSH) achieving a cumulative DexP delivery of about 20% and 18% respectively after 2 days. To better understand the process of drug release, the quantification of the BTC ligand of the MOF was also measured in PBS medium (Fig. 3c). Obviously, it followed the same trend as DexP, thereby indicating that the drug release is mainly driven by the degradation of MIL-100(Fe) at pH 7.4 due to the competitive substitution of BTC by phosphate from PBS in the coordination sphere of Fe^{3+} . A similar degradation process was previously described for pure MIL-100(Fe).^{26,37,51,52} The Fe release profile (Fig. 3d) is notably different from that of BTC release at pH 7.4 due presumably to the precipitation of iron phosphates as previously shown.^{51,52} In contrast, MIL-100(Fe) and $\text{Au}_{25}(13)@\text{MIL}$ present enhanced chemical stability under PBS acidic conditions (PBS and PBS + GSH at pH 5.1) and this can significantly control the kinetics

of DexP delivery. Such results indicate that a progressive DexP release from $\text{Au}_{25}(13)@\text{MIL}$ can thus be expected in intracellular compartments.

To mitigate the rapid DexP release at pH 7.4, the surface of the $\text{Au}_{25}@\text{MIL}$ nano-object was coated by a bioactive hyaluronic acid-polydopamine (HA-PDA) co-polymer (see the ESI† for details). HA has been extensively investigated for targeting cancer therapy due to its capacity of binding to the CD44 cell receptors.^{53–57} Since such cell receptors are also overexpressed on inflamed cells,⁵⁴ the HA-PDA co-polymer is prone to enhancing the targeting ability of $\text{Au}_{25}@\text{MIL}$ for inflammatory macrophages. The surface modified $\text{Au}_{25}(13)@\text{MIL}$ nano-object (*i.e.* $\text{Au}_{25}(13)@\text{MIL-HP}$) was synthesized following a procedure previously described for MIL-100(Fe).⁵⁸ Both HA-PDA and $\text{Au}_{25}(13)@\text{MIL-HP}$ were fully characterized as described in detail in the ESI (Fig. S13 and S14†). The surface modification of $\text{Au}_{25}(13)@\text{MIL}$ is expected to be mainly driven by strong coordination bonds between coordinatively unsaturated Fe sites on the surface of MIL-100(Fe) NPs and phenolic groups of HA-PDA. As shown by DLS results, the surface charge of $\text{Au}_{25}(13)@\text{MIL-HP}$ is more negative in the pH range of 4–8 in comparison with that of non-modified $\text{Au}_{25}(13)@\text{MIL}$ and meanwhile its hydrodynamic diameter of 146 ± 6 nm was very

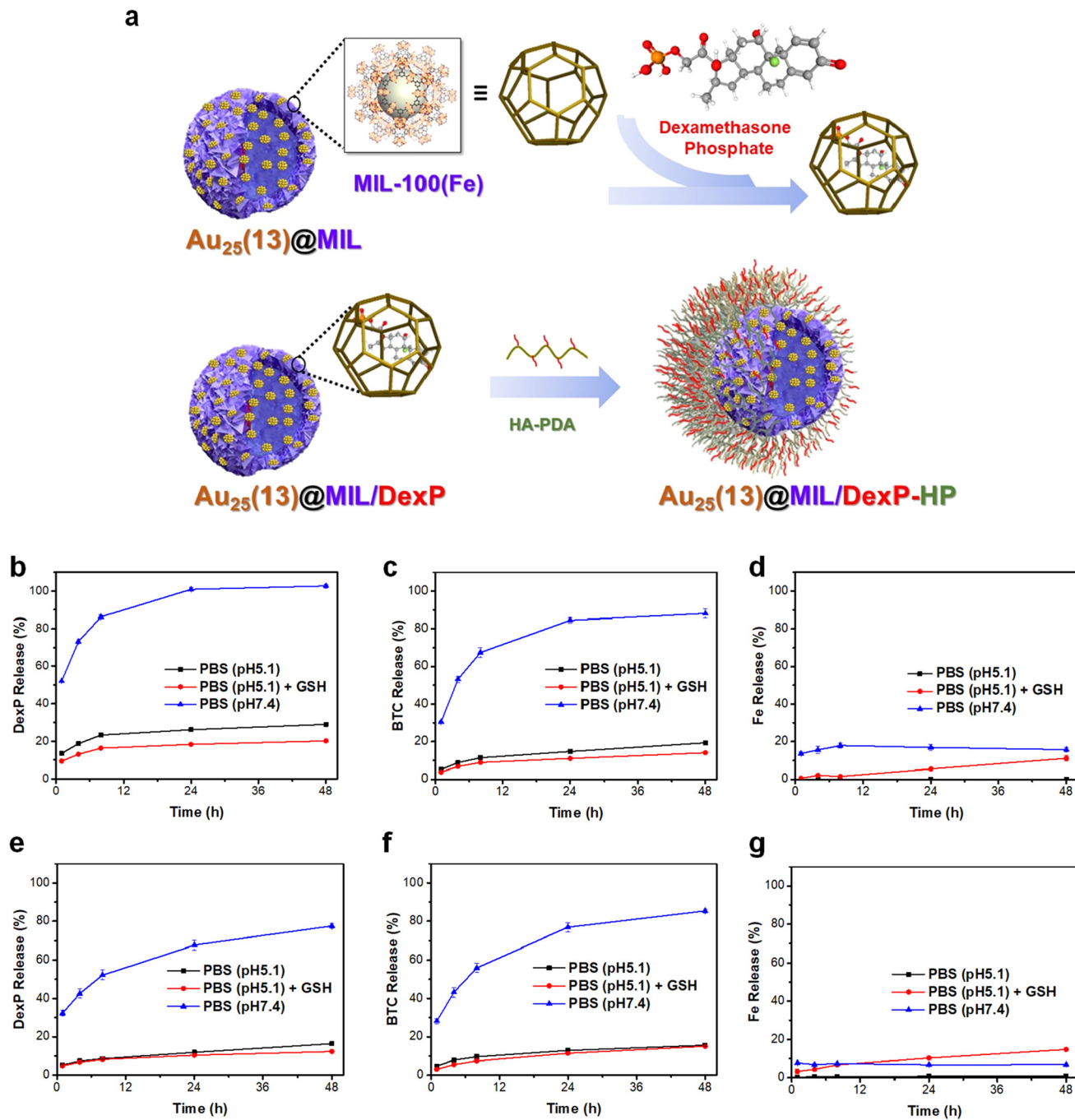


Fig. 3 (a) Scheme of the DexP loading in $\text{Au}_{25}(13)@\text{MIL}$ and its surface functionalization by HA-PDA; (b and e) DexP, (c and f) BTC and (d and g) Fe release from (b-d) $\text{Au}_{25}(13)@\text{MIL}/\text{DexP}$ and (e-g) $\text{Au}_{25}(13)@\text{MIL}/\text{DexP-HP}$ in different PBS media (*i.e.* PBS at pH 5.1, PBS at pH 5.1 with 10 mM GSH and PBS at pH 7.4). The DexP and BTC releases were measured by HPLC and the Fe release by ICP-MS. The experiments were performed in triplicate.

stable in that pH range, thereby showing the excellent colloidal stability of this nano-object (Fig. S15†). The release of DexP from $\text{Au}_{25}(13)@\text{MIL}/\text{DexP-HP}$ was substantially slowed down in neutral PBS in comparison with that in non-modified $\text{Au}_{25}(13)@\text{MIL}/\text{DexP}$. As shown in Fig. 3e, 52% DexP was delivered after 8 h from $\text{Au}_{25}(13)@\text{MIL}/\text{DexP-HP}$ at pH 7.4 while the delivery of DexP achieved 86% for non-modified $\text{Au}_{25}(13)$

$@\text{MIL}/\text{DexP}$ (Fig. 3b). However, the BTC release profile of $\text{Au}_{25}(13)@\text{MIL}/\text{DexP-HP}$ was similar to that of $\text{Au}_{25}(13)@\text{MIL}/\text{DexP}$ (Fig. 3c and f), revealing the fast degradation of the surface modified nano-object under neutral PBS conditions. The Fe release profile of $\text{Au}_{25}(13)@\text{MIL}/\text{DexP-HP}$ was also close to that of $\text{Au}_{25}(13)@\text{MIL}/\text{DexP}$ in different PBS media (Fig. 3g). The presence of HA-PDA chains at the surface of $\text{Au}_{25}(13)$

@MIL may additionally limit the accessibility of the mesopores of MIL-100(Fe) thereby slowing down the drug release kinetics.

2.3 *In vitro* cytotoxicity and macrophage internalization

The anti-inflammatory performance of the different MOF formulations developed in this study has been evaluated *in vitro* on monocytes and macrophages (see the Experimental section). The RAW 264.7 murine macrophage cell line was first co-incubated with different concentrations of $\text{Au}_{25}\text{SG}_{18}$ NCs, MIL-100(Fe), $\text{Au}_{25}(13)@\text{MIL}$, free DexP, $\text{Au}_{25}(13)@\text{MIL}/\text{DexP}$ and $\text{Au}_{25}(13)@\text{MIL}/\text{DexP-HP}$ for 24 h. The concentration of DexP was selected according to the DexP loading capacity of $\text{Au}_{25}(13)@\text{MIL}$. Except for the DexP treated group, the viability of the RAW 264.7 cells exposed to all other groups was around 80% up to the concentration of $50 \mu\text{g mL}^{-1}$ (Fig. S16a†), thereby showing that $\text{Au}_{25}\text{SG}_{18}$ NCs, MIL-100(Fe), $\text{Au}_{25}(13)@\text{MIL}$, $\text{Au}_{25}(13)@\text{MIL}/\text{DexP}$ and $\text{Au}_{25}(13)@\text{MIL}/\text{DexP-HP}$ present low cytotoxicity to normal macrophages. Lipopolysaccharide (LPS), a component of the outer membrane of Gram-negative bacteria is not only a key inflammatory factor but has also been frequently used to induce different models of inflammation.^{59,60} Indeed, LPS can bind to TLR4 and this recognition can trigger an inflammatory signaling cascade including NF- κ B and IRF, ultimately leading to the release of pro-inflammatory cytokines and the production of reactive oxygen species (ROS).^{59,60} Herein, LPS activated macrophages were then used as an *in vitro* inflammatory model. While the viability of LPS activated RAW 264.7 cells treated with DexP was similar to that of non-activated cells, exposure to MIL-100(Fe) and $\text{Au}_{25}(13)@\text{MIL}$ at concentration of $50 \mu\text{g mL}^{-1}$ decreased significantly the viability of inflammatory macrophages to 13% and 17%. Activated macrophages incubated with $\text{Au}_{25}(13)@\text{MIL}/\text{DexP}$ and $\text{Au}_{25}(13)@\text{MIL}/\text{DexP-HP}$ nano-objects exhibited a slightly higher viability of 30% (Fig. S16b†). Interestingly, these results highlight the selective toxicity of MIL-100(Fe) NPs and $\text{Au}_{25}@\text{MIL}$ based nano-objects for inflammatory cells in comparison with normal macrophages, which is not achieved by the free DexP drug.

To investigate the cellular uptake of $\text{Au}_{25}@\text{MIL}$ nano-objects and assess the role of HA-PDA coating, the cell internalization process was monitored by confocal laser scanning microscopy (CLSM) experiments at 0 h, 1 h, 4 h and 8 h post incubation (Fig. 4) in normal and LPS activated RAW 264.7 macrophages (see the Experimental section). The fluorescent dye rhodamine B (RhB) was encapsulated in the mesopores of $\text{Au}@\text{MIL}$ (denoted as $\text{Au}_{25}(13)@\text{MIL}/\text{RhB}$) and meanwhile the obtained $\text{Au}_{25}(13)@\text{MIL}/\text{RhB}$ was further coated with HA-PDA (denoted as $\text{Au}_{25}(13)@\text{MIL}/\text{RhB-HP}$). As shown by the profile of the fluorescence intensity in the cells (Fig. 4b and d), $\text{Au}_{25}(13)@\text{MIL}/\text{RhB-HP}$ showed a faster and higher internalization in activated macrophages in comparison with non-modified $\text{Au}_{25}(13)@\text{MIL}/\text{RhB}$. This is likely due to the binding of the HA-PDA copolymer to the CD44 receptor of these cells. In contrast, no significant difference in the internalization of both formulations was observed in the normal macrophages. Interestingly, the uptake of both $\text{Au}_{25}(13)@\text{MIL}/\text{RhB-HP}$ and

$\text{Au}_{25}(13)@\text{MIL}/\text{RhB}$ rapidly reached a plateau in non-activated macrophages, whereas it continuously increased in LPS activated RAW 264.7 macrophages over 8 hours. This uptake profile should be beneficial for their intrinsic anti-inflammatory properties with high selectivity towards activated macrophages and for targeted sustained drug release within inflammatory macrophages. Note that oral, local, and intravenous delivery can be employed for the administration of anti-inflammatory drugs. While the intravenous route allows the injection of the drug in the whole body, local delivery has also been found to be efficient as it enables to directly concentrate the drug into the inflamed tissues.^{22–26} Both oral and intravenous administration could therefore be envisaged for $\text{Au}_{25}(13)@\text{MIL}/\text{DexP-HP}$. The surface coating of $\text{Au}_{25}(13)@\text{MIL}/\text{DexP-HP}$ by using HA-PDA could confer an enhanced targeting ability and a progressive internalization towards inflammatory macrophages while the pH-responsive release properties of this nano-vector could be utilized to selectively and progressively deliver DexP to inflamed joints.

2.4 *In vitro* anti-inflammatory activity assay

In order to elucidate the mechanisms that are involved in the anti-inflammatory activity of $\text{Au}_{25}@\text{MIL}$, we performed additional screening of their anti-oxidative or anti-inflammatory properties. We first selected non-modified $\text{Au}_{25}(13)@\text{MIL}/\text{DexP}$ nano-objects since their cytotoxicity was found to be similar to that of the surface modified analogue (*i.e.* $\text{Au}_{25}(13)@\text{MIL}/\text{Dex-HP}$) (Fig. S16†). 2',7'-Dichlorofluorescein diacetate (DCF-DA) was thus used to evaluate the level of intracellular ROS present by confocal microscopy. As shown in Fig. S17,† a significant enhancement of fluorescence (directly proportional to ROS level) was observed in the LPS activated macrophages compared to normal ones, and the fluorescence decreased dramatically upon treatment with $\text{Au}_{25}(13)@\text{MIL}$, DexP and $\text{Au}_{25}(13)@\text{MIL}/\text{DexP}$. In contrast, incubation of activated macrophages with bare MIL-100(Fe) only slightly decreases their ROS level. These results confirmed the ability of $\text{Au}_{25}(13)@\text{MIL}$, DexP and $\text{Au}_{25}(13)@\text{MIL}/\text{DexP}$ to scavenge free radicals that are induced by LPS activation. Then, enzyme-linked immunosorbent assay (ELISA) was carried out to measure the secretion of pro-inflammatory cytokines in cell culture media. Among them, we focused on (i) TNF- α which is indicated in the proliferation of synovial fibroblasts, activation of osteoblasts, and destruction of cartilage and bone, (ii) IL-1 β that leads to cartilage metabolic disorder, bone absorption, and synovitis *via* promoting the release of other pro-inflammatory cytokines and proteinases and (iii) IL-6 that can induce the activation of synovial fibroblasts and osteoblasts, leading to articular cartilage and bone erosion.⁶¹ Activated RAW 264.7 were thus exposed to drug formulations of low concentrations to preclude the cell apoptosis mediated expression of pro-inflammatory cytokines. As shown in Fig. 5a–c, the concentrations of the three pro-inflammatory cytokines were remarkably decreased in the cell culture medium of activated macrophages exposed to DexP and $\text{Au}_{25}(13)@\text{MIL}/\text{DexP}$. Notably, $\text{Au}_{25}(13)@\text{MIL}/\text{DexP}$ showed better inhibition effects to the aforementioned proin-

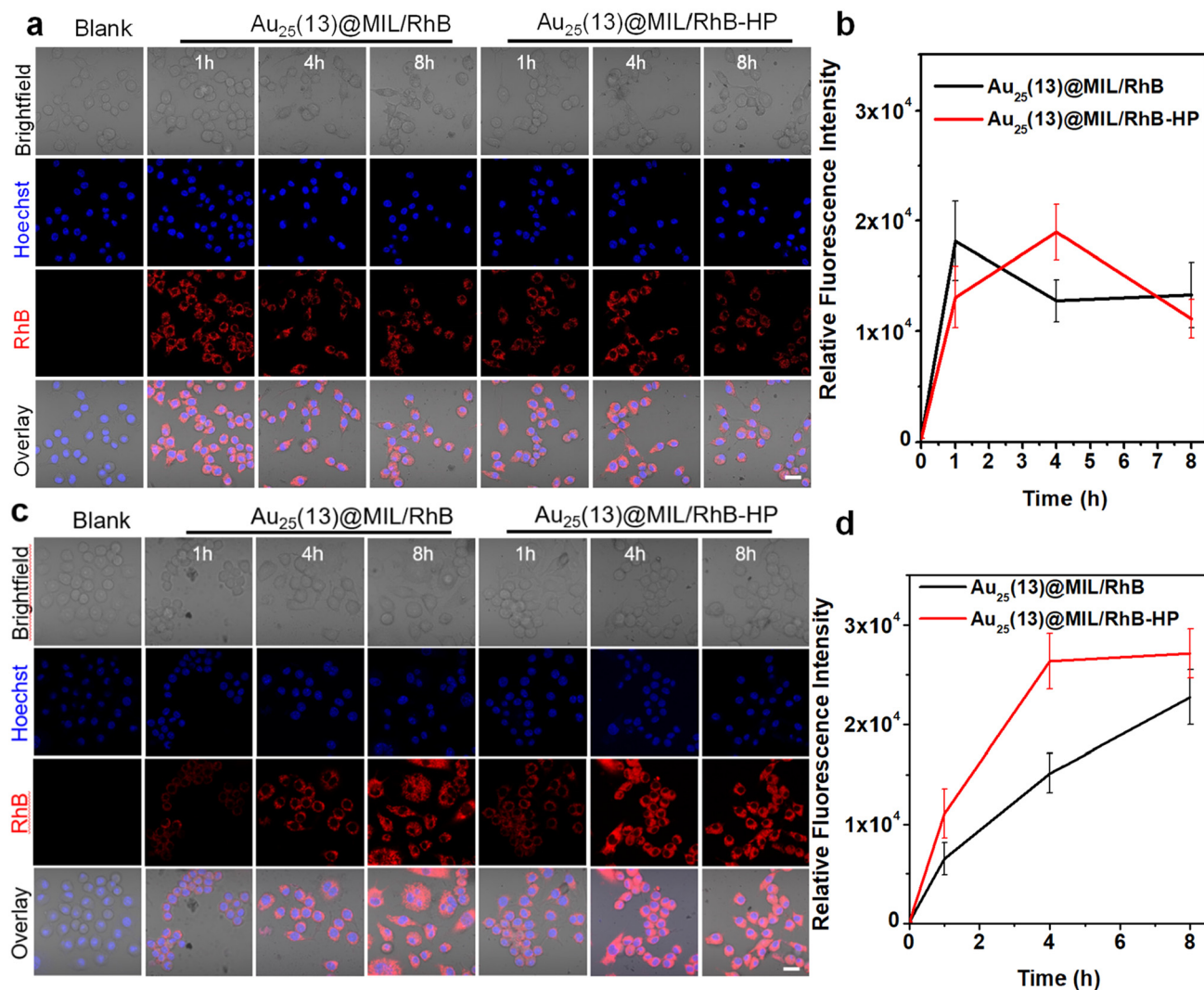


Fig. 4 Internalization of Au₂₅(13)@MIL/RhB and Au₂₅(13)@MIL/RhB-HP (50 $\mu\text{g mL}^{-1}$) by (a) normal RAW 264.7 macrophages and (c) LPS activated RAW 264.7 macrophages (LPS of 100 ng mL^{-1} , 48 h) as shown by CLSM. Scale bar = 20 μm ; (b and d) quantification of the intracellular relative fluorescence intensity of RhB as a function of the incubation time for (b) normal RAW 264.7 macrophages and (d) LPS activated RAW 264.7 macrophages with both nano-objects.

flammatory cytokines than MIL-100(Fe) and Au₂₅(13)@MIL. It is thus an excellent candidate to reduce the production of pro-inflammatory cytokines, in addition to its anti-oxidative effect. Herein, DexP and Au₂₅SG₁₈ NCs integrated in the Au₂₅(13)@MIL/DexP nano-object could serve as both anti-oxidants and pro-inflammatory cytokine regulation agents.

2.5 Inhibition of the TLR signaling by the Au₂₅(13)@MIL nano-object

To better shed light on the molecular signaling pathways that are regulated by our drug formulations, we used the THP1-DualTM human monocyte cell line, which is responsive to various stimuli that induce monocyte differentiation and activation.^{62–64} It is widely used as an *in vitro* model system for investigating the mechanisms underlying inflammatory diseases such as RA. It is known that the initiation and develop-

ment of RA involves abnormal signal transduction pathways of multiple cytokines.^{5,65} Due to the integration of two reporters (that is, secreted embryonic alkaline phosphatase (SEAP) and Lucia luciferase), the THP1-DualTM cell line allows the parallel monitoring of the NF- κ B and IRF signaling pathways. The latter are activated and upregulated through the binding of LPS to Toll-like receptors that play a central role in initiating the inflammatory response.^{5,65} The different mechanisms related to the activation NF- κ B have been well documented.^{65–68} Upon activation by LPS, NF- κ B translocates to the nucleus of macrophages where it induces the transcription of various genes that code for pro-inflammatory cytokines, chemokines and other inflammatory proteins.^{65–68} Attenuating TLR signaling has thus emerged as a novel therapeutic strategy for many inflammatory diseases.^{60,65–68} Note that glucocorticoids such as DexP are currently used in RA treatment as NF-

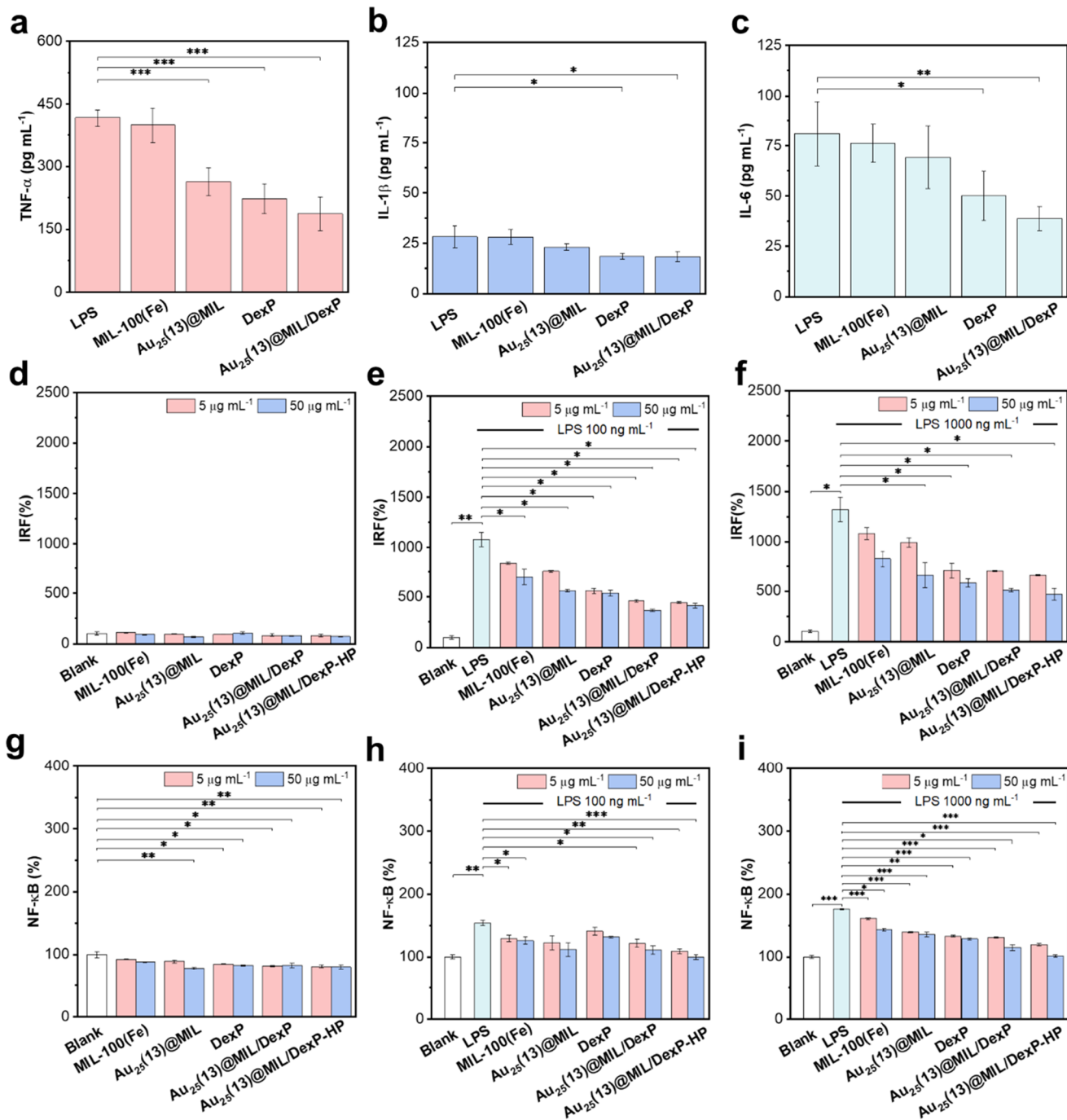


Fig. 5 Anti-inflammatory properties of $\text{Au}_{25}(13)@\text{MIL/DexP}$. (a–c) Concentrations of (a) TNF- α , (b) IL-1 β and (c) IL-6 pro-inflammatory cytokines in cell culture media measured by ELISA assay after the exposure of LPS activated RAW 264.7 macrophages (100 ng mL^{-1} , 48 h) to different formulations ($[\text{MIL-100(Fe)}] = 1 \text{ }\mu\text{g mL}^{-1}$, $[\text{Au}_{25}(13)@\text{MIL}] = 1 \text{ }\mu\text{g mL}^{-1}$, $[\text{DexP}] = 0.4 \text{ }\mu\text{g mL}^{-1}$, $[\text{Au}_{25}(13)@\text{MIL/DexP}] = 1 \text{ }\mu\text{g mL}^{-1}$) for 24 h; LPS induced (e and f) IRF and (h and i) NF- κB activation of THP1-DualTM cells incubated with different formulations (i.e. MIL-100(Fe), $\text{Au}_{25}(13)@\text{MIL}$, DexP, $\text{Au}_{25}(13)@\text{MIL/DexP}$ and $\text{Au}_{25}(13)@\text{MIL/DexP-HP}$ at the concentration of 5 or $50 \text{ }\mu\text{g mL}^{-1}$). The response of (d) IRF and (g) NF- κB signaling pathways without LPS stimulation is shown for comparison. IRF and NF- κB were quantified by using QUANTI-Luc and QUANTI-Blue, respectively. Results are shown as mean \pm SD. * $p < 0.05$, ** $p < 0.01$ and *** $p < 0.001$. The experiments were performed in triplicate.

κB inhibitors but they have endocrine and metabolic side effects when frequently administered.^{66–68}

The impact of $\text{Au}_{25}@\text{MIL}$ based formulations on TLR signaling was investigated by using THP1-DualTM monocytes that

were first differentiated into macrophage cells (M0) upon exposure to phorbol-12-myristate-13 acetate (PMA) and then treated with LPS (100 or 1000 ng mL^{-1}) for subsequent activation. Then, they were exposed to different drug formulations

at the concentration of 5 or 50 $\mu\text{g mL}^{-1}$. In contrast to RAW 264.7 cells, negligible cytotoxicity of all formulations to normal and activated THP-1 cells (with or without LPS) at a concentration as high as 50 $\mu\text{g mL}^{-1}$ was observed (Fig. S18a and b†). As shown in Fig. 5d–f, the IRF pathway is activated in a LPS dose-dependent manner. Without any stimulation of THP-1 cells by LPS, the activation of the IRF pathway was strongly limited, showing that these formulations are not able to trigger inflammation. However, free DexP, $\text{Au}_{25}(13)@\text{MIL}/\text{DexP}$ and $\text{Au}_{25}(13)@\text{MIL}/\text{DexP-HP}$ were able to significantly reduce the LPS-induced IRF activity. It is noteworthy that the LPS induced activation of IRF was more downregulated by $\text{Au}_{25}(13)@\text{MIL}/\text{DexP}$ and $\text{Au}_{25}(13)@\text{MIL}/\text{DexP-HP}$ than $\text{Au}_{25}(13)@\text{MIL}$ alone at the concentration of 50 $\mu\text{g mL}^{-1}$, further demonstrating their anti-inflammatory ability (Fig. 5e and f). The NF- κB pathway activation was shown to be less sensitive to the LPS dose (Fig. 5g–i). Surprisingly, DexP exhibited limited downregulation effects under LPS (100 ng mL^{-1}) activation. However, a significant decrease of NF- κB activation was observed for MIL-100(Fe), $\text{Au}_{25}(13)@\text{MIL}$, $\text{Au}_{25}(13)@\text{MIL}/\text{DexP}$ and $\text{Au}_{25}(13)@\text{MIL}/\text{DexP-HP}$ groups at the concentration of 50 $\mu\text{g mL}^{-1}$ under LPS (100 ng mL^{-1}) activation, suggesting that both nanoMOF and $\text{Au}_{25}\text{SG}_{18}$ components of $\text{Au}_{25}(13)@\text{MIL}/\text{DexP}$ play an inhibitor role in NF- κB activation. Therefore, in agreement with the cytokine production assays, $\text{Au}_{25}(13)@\text{MIL}/\text{DexP}$ and $\text{Au}_{25}(13)@\text{MIL}/\text{DexP-HP}$ can effectively downregulate TLR mediated IRF and NF- κB signaling pathways. Notably, the anti-inflammatory process was not strongly dose-dependent, since only a slight difference in the inhibition of both pathways was observed by varying the $\text{Au}_{25}(13)@\text{MIL}/\text{DexP}$ concentrations (5 and 50 $\mu\text{g mL}^{-1}$). As shown in Fig. S18† and Fig. 5, similar results were obtained for non-modified $\text{Au}(13)@\text{MIL}/\text{DexP}$ and $\text{Au}(13)@\text{MIL}/\text{DexP-HP}$. Thus, *in vitro* studies did not show any impact of HA-PDA coating of $\text{Au}_{25}@\text{MIL}$ nano-objects on their cytotoxicity and the inhibition of TLR signaling. Fig. 5 indicates also that free DexP is efficient in the inhibition of IRF signaling pathway. However, as previously described in the article, free DexP showed cytotoxicity to both normal and inflammatory macrophages while $\text{Au}(13)@\text{MIL}/\text{DexP-HP}$ possesses selective toxicity to inflammatory macrophages. Moreover, the presence of HA-PDA at the surface of $\text{Au}_{25}(13)@\text{MIL}/\text{DexP}$ can induce a targeted and progressive internalization of such nanovectors towards inflammatory macrophages and sustained DexP drug release.

3. Conclusion

An innovative therapeutic $\text{Au}_{25}@\text{MIL}$ nano-vector integrating the highly porous MIL-100(Fe) and atomically precise $\text{Au}_{25}\text{SG}_{18}$ NCs was synthesized through an *in situ* cost-effective and green protocol. This nano-object exhibited a tunable density of homogeneously dispersed $\text{Au}_{25}\text{SG}_{18}$ NCs within MIL-100(Fe) NPs. Due to its very low cytotoxicity and high loading

capacity of a glucocorticoid such as DexP, this nano-object was shown to be an interesting platform for the therapy of inflammatory diseases such as RA. The high anti-inflammatory capacity of $\text{Au}_{25}@\text{MIL}-\text{DexP}$ was fully demonstrated since this nano-object presented high cytotoxicity to activated macrophages and was able to scavenge intracellular ROS as well as reduce the secretion of pro-inflammatory cytokines. Interestingly, $\text{Au}_{25}@\text{MIL}-\text{DexP}$ was able to inhibit the LPS induced NF- κB and IRF signaling pathways. Note that the description of the signaling pathways involved in RA is not only of importance to understand the complex mechanisms at play but also is crucial for the identification of therapeutic targets and the development of novel drugs for RA. At the present time, most nanomedicines developed so far are single-target therapeutics. However, the pathogenesis of inflammatory diseases such as RA involves multiple mechanisms and factors and a nanomedicine capable of blocking simultaneously several signaling pathways may further improve the efficiency of the therapy.

4. Experimental section

4.1 Cells and culture conditions

RAW 264.7 macrophage cells were cultured in high glucose Dulbecco's modified Eagle's medium (DMEM) containing 10% FBS and 1% penicillin and streptomycin at 37 °C under a humidified 5% CO₂ atmosphere. THP1-DualTM cells were purchased from InvivoGen and were cultured in RPMI 1640 containing 10% FBS, 1% penicillin and streptomycin and 10 $\mu\text{g mL}^{-1}$ blasticidin, 100 $\mu\text{g mL}^{-1}$ ZeocinTM and 100 $\mu\text{g mL}^{-1}$ of NormocinTM at 37 °C under a humidified 5% CO₂ atmosphere according to the manufacturer's manual.

4.2 *In vitro* cytotoxicity assay

RAW 264.7 cells in the logarithmic phase were rinsed twice with PBS and then treated with a cell scraper to form 10⁵ per mL cell suspension. 100 μL of RAW 264.7 cell suspension was seeded in 96-well plates (10⁴ per well) and incubated overnight. Then, a different formula including DexP, MIL-100(Fe), $\text{Au}_{25}(13)@\text{MIL}$, $\text{Au}_{25}(13)@\text{MIL}/\text{DexP}$ and $\text{Au}_{25}(13)@\text{MIL}/\text{DexP-HP}$ in DMEM/FBS at different concentrations (1, 2, 5, 10, 20, 50 and 100 $\mu\text{g mL}^{-1}$) was added to each well, incubated for 24 hours at 37 °C and under 5% of CO₂. Note that the concentrations of MIL-100(Fe), $\text{Au}_{25}(13)@\text{MIL}$, $\text{Au}_{25}(13)@\text{MIL}/\text{DexP}$ and $\text{Au}_{25}(13)@\text{MIL}/\text{DexP-HP}$ were determined by the measurement of the residual mass after evaporation of a defined volume of colloidal suspension. 10 μL CCK-8 per well was added to the cells and after incubation for further 2 hours, the 96-well plate was transferred into a microplate reader (excitation at 450 nm) for UV-Vis absorbance analysis. The resulting UV-Vis absorbance values were normalized to the UV-Vis absorbance values of the control groups. All the experimental points were assessed triplicate, with error bars representing the standard error of the mean. The cell cytotoxicity of DexP and $\text{Au}_{25}(13)@\text{MIL}/\text{DexP}$

DexP was further studied on RAW 264.7 cells, following the same protocol.

$$\text{Cell viability (\%)} = \frac{A_{\text{Experimental group}} - A_{\text{Blank group}}}{A_{\text{Control group}} - A_{\text{Blank group}}} \times 100\%$$

4.3 Cellular uptake study by confocal laser scanning microscopy (CLSM)

The cellular uptake of $\text{Au}_{25}(13)@\text{MIL}$ and $\text{Au}_{25}(13)@\text{MIL-HP}$ was evaluated by CLSM on normal RAW 264.7 macrophages and LPS activated RAW 264.7 macrophages. $\text{Au}_{25}(13)@\text{MIL}$ was first labelled by a fluorescent dye rhodamine B (RhB). Typically, 1 mL of RhB aqueous solution (1 mg mL⁻¹) was added to 5 mg of $\text{Au}_{25}(13)@\text{MIL}$ under stirring at 600 rpm for 24 h. After centrifugation and washing with Milli Q water repeatedly, the resulting $\text{Au}_{25}(13)@\text{MIL/RhB}$ was redispersed in 5 mL Milli Q water with tin foil covering and kept at 4 °C in a refrigerator until use. As for the synthesis of $\text{Au}_{25}(13)@\text{MIL/RhB-HP}$, an extra step was to mix $\text{Au}_{25}(13)@\text{MIL/RhB}$ with HA-PDA at the weight ratio of 1 : 1. RAW 264.7 cells were seeded into 35 mm confocal dishes (1 × 10⁵ cells per mL) and maintained overnight. For LPS activated RAW 264.7 macrophages, cells were first treated with 100 ng mL⁻¹ LPS for 48 h and then the medium was replaced with fresh complete medium containing $\text{Au}_{25}(13)@\text{MIL/RhB}$ (50 µg mL⁻¹) or $\text{Au}_{25}(13)@\text{MIL/RhB-HP}$ (50 µg mL⁻¹), followed by an incubation at 37 °C for 1 h, 4 h and 8 h. As for CLSM imaging, after the removal of the MOF containing media, the nucleus was stained by Hoechst. Then, the as prepared samples were imaged by CLSM (ZEISS LSM780, Germany). The laser excitation wavelength was 543 nm.

4.4 Inhibition of inflammatory macrophages

Similar to the *in vitro* cytotoxicity assay, *in vitro* anti-inflammatory study was based on inflammatory macrophages after activation with LPS. After adhesion overnight, RAW 264.7 cells were treated with LPS for 48 h before their incubation with $\text{Au}_{25}(13)@\text{MIL}$, DexP, $\text{Au}_{25}(13)@\text{MIL/DexP}$ and $\text{Au}_{25}(13)@\text{MIL/DexP-HP}$ in DMEM/FBS at different concentrations (1, 2, 5, 10, 20, 50 and 100 µg mL⁻¹). After one day's incubation, 10 µL of CCK-8 was added to each well for measurement of UV-Vis absorbance. The survival rate of inflammatory cells was thus compared.

4.5 ROS scavenging properties

To investigate the reactive oxygen species (ROS) scavenging capacity, RAW 264.7 cells were incubated with different formulations (MIL-100(Fe), $\text{Au}_{25}(13)@\text{MIL}$, DexP and $\text{Au}_{25}(13)@\text{MIL/DexP}$) in the presence of LPS at a concentration of 100 ng mL⁻¹ for 24 h. After the removal of the aforementioned materials containing the supernatant, fresh serum-free medium containing dichlorofluorescein diacetate (DCF-DA, 10 µM) for ROS imaging and Hoechst for nucleus staining was added for 30 min in the dark. A confocal laser microscope was used to detect intracellular ROS level. The intensity of green fluorescence indicates the intracellular ROS level.

4.6 Pro-inflammatory cytokine downregulation

To investigate the downregulation effect of pro-inflammatory cytokines of DexP loaded $\text{Au}_{25}(13)@\text{MIL}$, RAW 264.7 cells were seeded at a density of 1 × 10⁵ cells per mL into a 6-well plate and incubated at 37 °C under 5% CO₂ overnight and then the cells were incubated with LPS at a concentration of 100 ng mL⁻¹ for 48 h. After this activation step, DMEM was replaced by fresh DMEM containing MIL-100(Fe), $\text{Au}_{25}(13)@\text{MIL}$, and $\text{Au}_{25}(13)@\text{MIL/DexP}$ at a concentration of 1 µg mL⁻¹. For comparison, activated RAW 264.7 cells were exposed to free DexP at a concentration of 0.4 µg mL⁻¹ for 24 hours. The amount of free DexP is based on the drug loading in the nanocarrier $\text{Au}_{25}(13)@\text{MIL}$, namely the equivalent drug. Note that the dose of DexP in $\text{Au}_{25}(13)@\text{MIL}$ was comparable to that of Dex formulations whose inhibitory effect on pro-inflammatory cytokine secretion has been previously studied.^{1–6}

Then, the supernatant was collected and centrifuged to remove cells pellets and materials for next step detection. Briefly, mouse tumor necrosis factor alpha (TNF-α) DY410 DuoSet® ELISA, R&D Systems; mouse interleukin 1 beta (IL-1β) DY401 DuoSet® ELISA, R&D Systems; and mouse interleukin 6 (IL-6) DY406 DuoSet ELISA, R&D Systems were used to access TNF-α, IL-1β, and IL-6 concentrations from cell culture media samples by the standard ELISA technique, namely sandwich ELISA (capture antibody + sample or standard + detection antibody). Following the manufacturer's instructions, the samples were finally diluted five times for ELISA based on absorbance values of the recombinant mouse standard.

4.7 NF-κB and IRF pathway blockade

The THP1-Dual™ cell line allowed the simultaneous study of the NF-κB pathway, by monitoring the activity of secreted embryonic alkaline phosphatase (SEAP), and the interferon regulatory factor (IRF) pathway by assessing the activity of Lucia luciferase. Similarly to the cytotoxicity study, THP1-Dual™ cells were seeded into a 24-well plate at a density of 5 × 10⁵ cells per mL with phorbol-12-myristate-13 acetate (PMA) (50 ng mL⁻¹) to adhere for two days and differentiate into macrophages. Subsequently, adherent THP1-Dual™ cells were treated with different formulae (DexP, MIL-100(Fe), $\text{Au}_{25}(13)@\text{MIL}$, $\text{Au}_{25}(13)@\text{MIL/DexP}$ and $\text{Au}_{25}(13)@\text{MIL/DexP-HP}$) with or without LPS (100 or 1000 ng mL⁻¹) for 24 hours. Firstly, the cell viability of THP1-Dual™ cells was analyzed using a CCK-8 assay kit. After 2 h of incubation, cell viability was determined by the intensity of 590 nm emission under the excitation of 550 nm. In a parallel experiment, the supernatant was collected after one step of centrifugation (500g, 5 min) to remove floating cells pellets and materials. Following the manual's procedures, NF-κB and IRF induction and luciferase activity in the supernatant were quantified by QUANTI-Blue (InvivoGen) and QUANTI-Luc (InvivoGen), respectively. In detail, to measure NF-κB induction, 20 µL of the supernatant from the cell plate was incubated with 180 µL of QUANTI-Blue solution per well in a transparent 96 well plate for 3 h at 37 °C and the UV-Vis absorbance at 655 nm was measured using SpectraMax

iD3 multimode plate reader (Molecular Devices, CA, USA). To measure IRF induction, 10 μ L of the sample was incubated with 50 μ L of QUANTI-Luc solution per well in an opaque 96 well plate and the luminescence was measured using SpectraMax iD3 multimode plate reader (Molecular Devices, CA, USA). Changes from baseline were calculated as-fold changes, normalized against unstimulated control cells.

4.8 Statistical analysis

All experimental results were exhibited as the mean \pm standard deviation and the statistical significance among the groups was analyzed using one-way ANOVA, followed by LSD or Dunnett T3 *post hoc* test. SPSS 26.0 software was used for statistical analysis. Differences with a p value < 0.05 were considered to be statistically significant. Statistical significance was assigned for $*p < 0.05$, $**p < 0.01$ and $***p < 0.001$.

Author contributions

H. Z. optimized the synthesis and structural characterization of nano-objects, performed the drug encapsulation and all *in vitro* cell experiments. H. Z. wrote the first draft of the manuscript. S. B., S. M. and F. C. supervised *in vitro* cell experiments. G. P. performed TEM experiments and their analysis. E. D., F. G., C. S. and N. S. conceptualized the work, supervised the project and were involved in data analysis. N.S. was involved in the writing and editing of the manuscript with the contribution of all authors.

Conflicts of interest

The authors declare no conflict of interest.

Acknowledgements

H. Z. is grateful for the support from the CSC grant (grant number 201808320434). The authors would like to thank Shan Dai at ENS for the constructive discussion, Bernard Goetz at ENS for the measurement of ICP-MS, and Xiangzhen Xu at ESPCI for the help in TEM observation. F. G. and S. B. are thankful to Jean Philippe Herbeval for providing the THP1-DualTM cells. This work was supported by the IdEx Université Paris Cité, ANR-18-IDEX-0001 (IVETh plateform), by the Region Ile de France under the convention SESAME 2019 – IVETh (EX047011) (IVETh plateform), by the Région Ile de France and Banque pour l'Investissement (BPI) under the convention Accompagnement et transformation des filières projet de recherche et développement no. DOS0154423/00 & DOS0154424/00 (IVETh platform), and Agence Nationale de la Recherche through the program France 2023 “Integrateur biothérapie-bioproduction” (ANR-22-AIBB-000).

References

- 1 R. Medzhitov, *Nature*, 2008, **454**, 428–435.
- 2 D. M. Lee and M. E. Weinblatt, *Lancet*, 2001, **358**, 903–911.
- 3 G. S. Firestein, *Nature*, 2003, **423**, 356–361.
- 4 R. Brusini, M. Varna and P. Couvreur, *Adv. Drug Delivery Rev.*, 2020, **157**, 161–178.
- 5 S. Liu, H. Ma, H. Zhang, C. Deng and P. Xin, *Clin. Immunol.*, 2021, **230**, 108793.
- 6 M. Zheng, H. Jia, H. Wang, L. Liu, Z. He, Z. Zhang, W. Yang, L. Gao, X. Gao and F. Gao, *RSC Adv.*, 2021, **11**, 7129–7137.
- 7 Z. Sun, T. Li, T. Mei, Y. Liu, K. Wu, W. Le and Y. Hu, *J. Mater. Chem. B*, 2023, **11**, 3273–3294.
- 8 D. Xu, Q. Duan, H. Yu and W. Dong, *J. Mater. Chem. B*, 2023, **11**, 5976–5989.
- 9 Z. Lin, D. Liao, C. Jiang, A. Nezamzadeh-Ejhieh, M. Zheng, H. Yuan, J. Liu, H. Song and C. Lu, *RSC Med. Chem.*, 2023, **14**, 1914–1933.
- 10 K. Lu, T. Aung, N. Guo, R. Weichselbaum and W. Lin, *Adv. Mater.*, 2018, **30**, 1707634.
- 11 L. Wang, M. Zheng and Z. Xie, *J. Mater. Chem. B*, 2018, **6**, 707–717.
- 12 M.-X. Wu and Y.-W. Yang, *Adv. Mater.*, 2017, **29**, 1606134.
- 13 I. Abánades Lázaro and R. S. Forgan, *Coord. Chem. Rev.*, 2019, **380**, 230–259.
- 14 X. Ma, M. Lepoitevin and C. Serre, *Mater. Chem. Front.*, 2021, **5**, 5573–5594.
- 15 W. Cai, C.-C. Chu, G. Liu and Y.-X. Wang, *Small*, 2015, **11**, 4806–4822.
- 16 F. Demir Duman and R. S. Forgan, *J. Mater. Chem. B*, 2021, **9**, 3423–3449.
- 17 J. W. M. Osterrieth and D. Fairen-Jimenez, *Biotechnol. J.*, 2021, **16**, 2000005.
- 18 W. Zhu, J. Zhao, Q. Chen and Z. Liu, *Coord. Chem. Rev.*, 2019, **398**, 113009.
- 19 H. Zhao, C. Serre, E. Dumas and N. Steunou, in *Metal-Organic Frameworks for Biomedical Applications*, ed. M. Mozafari, Elsevier, 2020, ch. 18, pp. 397–423.
- 20 M. Peller, K. Böll, A. Zimpel and S. Wuttke, *Inorg. Chem. Front.*, 2018, **5**, 1760–1779.
- 21 H. Zhang, Y. Shang, Y.-H. Li, S.-K. Sun and X.-B. Yin, *ACS Appl. Mater. Interfaces*, 2019, **11**, 1886–1895.
- 22 L. Guo, Y. Chen, T. Wang, Y. Yuan, Y. Yang, X. Luo, S. Hu, J. Ding and W. Zhou, *J. Controlled Release*, 2021, **330**, 119–131.
- 23 Y. Wang, T. Ying, J. Li, Y. Xu, R. Wang, Q. Ke, S. G. F. Shen, H. Xu and K. Lin, *Chem. Eng. J.*, 2020, **402**, 126273.
- 24 Y. Yin, J. Yang, Y. Pan, Y. Gao, L. Huang, X. Luan, Z. Lin, W. Zhu, Y. Li and Y. Song, *Adv. Healthcare Mater.*, 2021, **10**, 2000973.
- 25 F. Zhou, J. Mei, S. Yang, X. Han, H. Li, Z. Yu, H. Qiao and T. Tang, *ACS Appl. Mater. Interfaces*, 2020, **12**, 2009–2022.
- 26 H. Zhao, S. Sene, A. M. Mielcarek, S. Miraux, N. Menguy, D. Ihiawakrim, O. Ersen, C. Pechoux, N. Guillou, J. Scola, J. M. Grelon, F. Nouar, S. Mura, F. Carn, F. Gazeau,

E. Dumas, C. Serre and N. Steunou, *J. Mater. Chem. B*, 2023, **11**, 3195–3211.

27 Q. Yuan, F. Gao, Y. Yao, P. Cai, X. Zhang, J. Yuan, K. Hou, L. Gao, X. Ren and X. Gao, *Theranostics*, 2019, **9**, 1825–1836.

28 M. F. Hornos Carneiro and F. Barbosa, Jr., *J. Toxicol. Environ. Health, Part B*, 2016, **19**, 129–148.

29 A. Saad, S. Biswas, E. Gkaniatsou, C. Sicard, E. Dumas, N. Menguy and N. Steunou, *Chem. Mater.*, 2021, **33**, 5825–5849.

30 M. Panchal, F. Nouar, C. Serre, M. Benzaquim, S. Sene, N. Steunou and M. Giménez Marqués, *US Pat.*, 20210277042, 2021.

31 A. Permyakova, A. Kakar, J. Bachir, E. Gkaniatsou, B. Haye, N. Menguy, F. Nouar, C. Serre, N. Steunou, T. Coradin, F. M. Fernandes and C. Sicard, *ACS Mater. Lett.*, 2023, **5**, 79–84.

32 Y. Shichibu, Y. Negishi, H. Tsunoyama, M. Kanehara, T. Teranishi and T. Tsukuda, *Small*, 2007, **3**, 835–839.

33 Y. Negishi, K. Nobusada and T. Tsukuda, *J. Am. Chem. Soc.*, 2005, **127**, 5261–5270.

34 P. Horcajada, S. Surble, C. Serre, D.-Y. Hong, Y.-K. Seo, J.-S. Chang, J.-M. Grenèche, I. Margiolaki and G. Férey, *Chem. Commun.*, 2007, 2820–2822.

35 S. Qi, H. S. Al-mashriqi, A. Salah and H. Zhai, *Microchem. J.*, 2022, **175**, 107163.

36 W. Dong, J. Yu, X. Gong, W. Liang, L. Fan and C. Dong, *Spectrochim. Acta, Part A*, 2021, **247**, 119085.

37 S. Sene, M. T. Marcos-Almaraz, N. Menguy, J. Scola, J. Volatron, R. Rouland, J.-M. Grenèche, S. Miraux, C. Menet, N. Guillou, F. Gazeau, C. Serre, P. Horcajada and N. Steunou, *Chem.*, 2017, **3**, 303–322.

38 E. Bellido, M. Guillevic, T. Hidalgo, M. J. Santander-Ortega, C. Serre and P. Horcajada, *Langmuir*, 2014, **30**, 5911–5920.

39 S. Shen, Y. Wu, Y. Liu and D. Wu, *Int. J. Nanomed.*, 2017, **12**, 4085–4109.

40 J. Ran, H. Zeng, J. Cai, P. Jiang, P. Yan, L. Zheng, Y. Bai, X. Shen, B. Shi and H. Tong, *Chem. Eng. J.*, 2018, **333**, 20–33.

41 C. Sarkar, A. R. Chowdhuri, S. Garai, J. Chakraborty and S. K. Sahu, *Cellulose*, 2019, **26**, 7253–7269.

42 T. Xiao, L. Fan, R. Liu, X. Huang, S. Wang, L. Xiao, Y. Pang, D. Li, J. Liu and Y. Min, *ACS Appl. Mater. Interfaces*, 2021, **13**, 50836–50850.

43 M. G. Bello, Y. Yang, C. Wang, L. Wu, P. Zhou, H. Ding, X. Ge, T. Guo, L. Wei and J. Zhang, *Part. Part. Syst. Charact.*, 2020, **37**, 2000147.

44 K. Zhao, T. Guo, C. Wang, Y. Zhou, T. Xiong, L. Wu, X. Li, P. Mittal, S. Shi, R. Gref and J. Zhang, *Acta Pharm. Sin. B*, 2020, **10**, 1709–1718.

45 N. Liang, N. Ren, Z. Feng, Z. Sun, M. Dong, W. Wang, F. Liu, C. Sun, W. Zhou, Z. Xing, J. Wang, C. Liu and H. Liu, *Adv. Healthcare Mater.*, 2022, **11**, 2102821.

46 M. d. J. Velásquez-Hernández, R. Ricco, F. Carraro, F. T. Limpoco, M. Linares-Moreau, E. Leitner, H. Wiltsche, J. Rattenberger, H. Schröttner, P. Frühwirt, E. M. Stadler, G. Gescheidt, H. Amenitsch, C. J. Doonan and P. Falcaro, *CrystEngComm*, 2019, **21**, 4538–4544.

47 V. Agostoni, T. Chalati, P. Horcajada, H. Willaime, R. Anand, N. Semiramoth, T. Baati, S. Hall, G. Maurin, H. Chacun, K. Bouchemal, C. Martineau, F. Taulelle, P. Couvreur, C. Rogez-Kreuz, P. Clayette, S. Monti, C. Serre and R. Gref, *Adv. Healthcare Mater.*, 2013, **2**, 1630–1637.

48 Y. Wang, J. Yan, N. Wen, H. Xiong, S. Cai, Q. He, Y. Hu, D. Peng, Z. Liu and Y. Liu, *Biomaterials*, 2020, **230**, 119619.

49 S. Mura, J. Nicolas and P. Couvreur, *Nat. Mater.*, 2013, **12**, 991–1003.

50 N. Ballatori, S. M. Krance, S. Notenboom, S. Shi, K. Tieu and C. L. Hammond, *Biol. Chem.*, 2009, **390**, 191–214.

51 I. Christodoulou, T. Bourguignon, X. Li, G. Patriarche, C. Serre, C. Marlière and R. Gref, *Nanomaterials*, 2021, **11**, 722.

52 X. Li, L. Lachmanski, S. Safi, S. Sene, C. Serre, J. M. Grenèche, J. Zhang and R. Gref, *Sci. Rep.*, 2017, **7**, 13142.

53 K. Kim, H. Choi, E. S. Choi, M.-H. Park and J.-H. Ryu, *Pharmaceutics*, 2019, **11**, 301.

54 S. S. M. Lee-Sayer, Y. Dong, A. A. Arif, M. Olsson, K. L. Brown and P. Johnson, *Front. Immunol.*, 2015, **6**, 150.

55 H. Lee, S. M. Dellatore, W. M. Miller and P. B. Messersmith, *Science*, 2007, **318**, 426–430.

56 P. Yang, F. Zhu, Z. Zhang, Y. Cheng, Z. Wang and Y. Li, *Chem. Soc. Rev.*, 2021, **50**, 8319–8343.

57 Z. Wang, Y. Duan and Y. Duan, *J. Controlled Release*, 2018, **290**, 56–74.

58 Y. Zhang, L. Wang, L. Liu, L. Lin, F. Liu, Z. Xie, H. Tian and X. Chen, *ACS Appl. Mater. Interfaces*, 2018, **10**, 41035–41045.

59 K. Lucas and M. Maes, *Mol. Neurobiol.*, 2013, **48**, 190–204.

60 H. Yang, S.-Y. Fung, S. Xu, D. P. Sutherland, T. R. Kollmann, M. Liu and S. E. Turvey, *ACS Nano*, 2015, **9**, 6774–6784.

61 C. Orr, E. Vieira-Sousa, D. L. Boyle, M. H. Buch, C. D. Buckley, J. D. Canete, A. I. Catrina, E. H. S. Choy, P. Emery, U. Fearon, A. Filer, D. Gerlag, F. Humby, J. D. Isaacs, S. A. Just, B. R. Lauwers, B. Le Goff, A. Manzo, T. McGarry, I. B. McInnes, A. Najm, C. Pitzalis, A. Pratt, M. Smith, P. P. Tak, S. W. Tas, R. Thurlings, J. E. Fonseca and D. J. Veale, *Nat. Rev. Rheumatol.*, 2017, **13**, 463–475.

62 A. Bastin, A. Sadeghi, M. H. Nematollahi, M. Abolhassani, A. Mohammadi and H. Akbari, *J. Cell Physiol.*, 2021, **236**, 2790–2799.

63 J. Auwerx, *Experientia*, 1991, **47**, 22–31.

64 Z. Qin, *Atherosclerosis*, 2012, **221**, 2–11.

65 A. Roy, M. Srivastava, U. Saqib, D. Liu, S. M. Faisal, S. Sugathan, S. Bishnoi and M. S. Baig, *Int. Immunopharmacol.*, 2016, **40**, 79–89.

66 A. Oeckinghaus, M. S. Hayden and S. Ghosh, *Nat. Immunol.*, 2011, **12**, 695–708.

67 T. Liu, L. Zhang, D. Joo and S.-C. Sun, *Signal Transduction Targeted Ther.*, 2017, **2**, e17023.

68 P. J. Barnes and M. Karin, *N. Engl. J. Med.*, 1997, **336**, 1066–1071.